Disentangling contributions of point and line defects in the Raman spectra of graphene-related materials

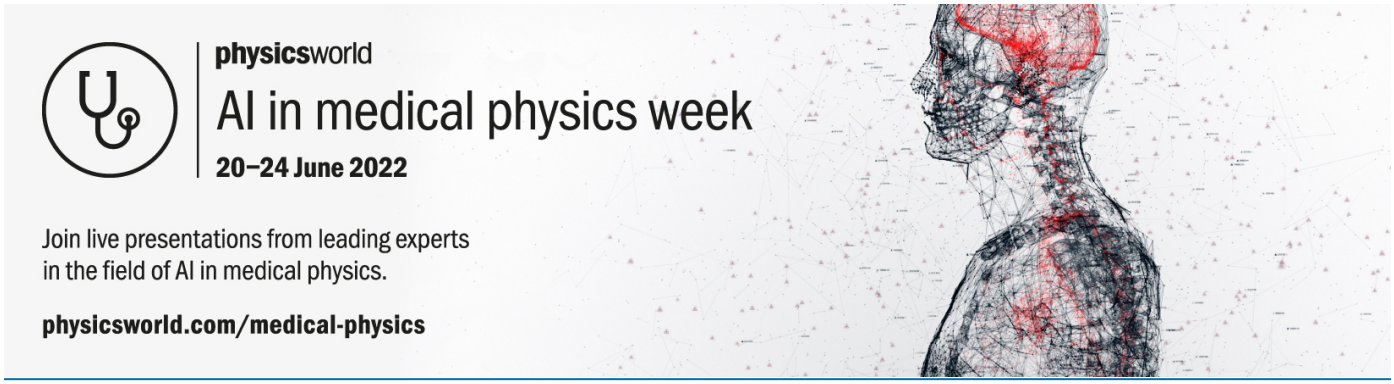

2D Materials

OPEN ACCESS

RECEIVED
13 November 2016

REVISED
10 January 2017

ACCEPTED FOR PUBLICATION
25 January 2017

PUBLISHED
24 February 2017

PAPER

Disentangling contributions of point and line defects in the Raman spectra of graphene-related materials

Luiz Gustavo Cançado[1], Mateus Gomes da Silva[1], Erlon H Martins Ferreira[2], Ferdinand Hof[3], Katerina Kampioti[3], Kai Huang[3], Alain Pénicaud[3], Carlos Alberto Achete[2], Rodrigo B Capaz[4] and Ado Jorio[1]

[1] Departamento de Física, Universidade Federal de Minas Gerais, Belo Horizonte, MG 31.270-901, Brazil
[2] Divisão de Metrologia de Materiais-DIMAT, Instituto Nacional de Metrologia, Qualidade e Tecnologia-INMETRO, Xerém, Duque de Caxias, RJ 25250-020, Brazil
[3] Centre de Recherche Paul Pascal—CNRS, UPR 8641, Université Bordeaux–I, 33600 Pessac, France
[4] Instituto de Física, Universidade Federal do Rio de Janeiro, Caixa Postal 68528, Rio de Janeiro, RJ 21941-972, Brazil

E-mail: adojorio@fisica.ufmg.br

Keywords: graphene, Raman, defects

Abstract

The transition from graphene to a fully disordered sp^2 carbon material can be idealized by either cutting graphene into smaller and smaller pieces, or adding more and more point defects. In other words, from the dimensionality standpoint, defects in two-dimensional (2D) systems can be either one- (1D) or zero-dimensional (0D). From an application point of view, both in terms of bottom-up as well as top-down approaches, the discrimination between these two structural disorder in two-dimensional systems is urgently desired. In graphene, both types of defects produce changes in the Raman spectrum, but identifying separately the contribution from each defect-type has not yet been achieved. Here we show that a diagram can be built for disentangling contributions of point-like and line-like defects to the Raman spectra of graphene-related materials embracing, from the topology point of view, all possible structures from perfect to fully disordered sp^2 bonded carbons. Two sets of graphene-related samples, produced by well-established protocols that generate either 0D or 1D defects in a controlled way, are analysed with our model and used to parameterize the limiting values of the phase space. We then discuss the limitations and apply our new methodology to analyse the structure of two-dimensional nanocarbons generated from renewable gas, used to produce inks and conducting coatings.

1. Introduction

In two-dimensional (2D) lattices, defects can be either zero-dimensional (0D), such as vacancies, dopants or functional chemical groups, or one-dimensional (1D), such as dislocations or crystallite borders, the latter appearing during growth and enclosing a crystallite area [1, 2]. This simple geometrical distinction determines defect functionality and their influence on materials properties [3–7]. Defects in the 2D sp^2 honeycomb carbon lattice dictate structural amorphization from pristine graphene or graphite down to more complex structures, such as amorphous carbon, black carbon, charcoal, biochar or, to a larger extent, organic molecules. One can idealize the transition from graphene to amorphous sp^2 carbon materials either by cutting graphene into smaller and smaller pieces, or by adding more and more point defects.

From the synthesis procedures to the integration of graphene into devices, from amorphous carbon to highly oriented pyrolytic graphite (HOPG), Raman spectroscopy is the preferred tool to identify and quantify defects [8–33]. Structural characterization of defects in graphene by Raman spectroscopy has already produced well-established protocols for the quantification of both point-defect concentrations [19, 20, 24] and crystallite sizes [14, 30] separately. However, most graphene samples, e.g. generated by chemical vapor deposition (CVD) or liquid phase exfoliation, are likely to exhibit both types of defects, and a method to disentangle and differentiate between 0D and 1D defects in such systems has not been developed until now. Here we show it is possible to disentangle the contribution of defects with distinct dimensionalities in the sp^2 carbon Raman spectra. We develop a procedure that enables researchers to use Raman spectroscopy to

determine quantitatively and simultaneously point-defect concentration and crystallite size in graphene-related materials, a necessary tool to study the effect of point and line defects on the properties of carbon sp^2 materials. The methodology has limitations, mostly for samples with low defect concentrations, where doping, strain and number of layers add significant additional parameters that have to be taken into account to properly parameterize the protocol proposed here. Otherwise, the procedure may help to identify suitable starting carbon materials for dispersion, or for materials applications, and also to adjust process parameters to boost properties such as electrical and thermal conductivity in deposited graphene films.

2. Statement of the problem

To identify the spectral features that allow the disentanglement of 0D and 1D defects in the Raman spectrum of graphitic materials, we studied 25 different graphene samples, grouped in two sets. These two sets correspond to standard reference materials varying from pristine 2D hexagonal sp^2 carbon lattices to highly disordered structures, following two different routes:

- Sample set 1 starts as pristine graphene prepared by the mechanical exfoliation method of HOPG, and it is ion-bombarded with different ion doses, generating an increasing number of 0D defects, down to a fully disordered structure [19, 20, 24]. From now on these samples are referred to as 'samples with point-defects', and they are characterized by the average distance between nearest defects (L_D) or by the defect density ($\sigma = 1/L_D^2$). This type of system is illustrated in figure 1(a). Pristine graphene has $L_D \rightarrow \infty$, and fully disordered graphene has $L_D \rightarrow 0$;
- Sample set 2 starts as a fully amorphous carbon material prepared by laser ablation of HOPG, and it is heat treated at different temperatures, thus generating sp^2 crystalline structures of increasingly larger crystallite sizes, up to a highly crystalline turbostratic graphitic structure for the highest heat treatment temperature [14, 30]. Geometrically, this sample can be thought as a graphene layer 'cut' by several 1D defects, or an ensemble of nanographite crystallites delimited by their borders, as illustrated in figure 1(b). From now on these samples are referred to as 'samples with line-defects', and they are characterized by their average crystallite size (L_a), or by the crystallite area (L_a^2). Pristine graphene has $L_a \rightarrow \infty$, and fully disordered graphene has $L_a \rightarrow 0$.

To date, these two sets of samples have been treated separately in Raman spectroscopy studies. The most ordinary protocols are based on the intensity ratio between the disorder-induced D band ($\sim 1350\,cm^{-1}$) and the first-order allowed bond-stretching G band ($\sim 1580\,cm^{-1}$), namely I_D/I_G. As in [14, 30] we use the integrated intensity (peak area) ratio rather than the intensity ratio, because the area under each peak represents the probability of the process, and the differences between the spectral information from samples with point versus line defects are better represented. Different from our previous publications [14, 30], here we use A_D/A_G rather than I_D/I_G to make it clear we are accounting for the area ratio.

These protocols are summarized in figures 1(c) and (d), which present theoretical plots of A_D/A_G as a function of L_D [19, 24] and L_a [14, 30], respectively, for three distinct values of excitation laser energies, E_L (see figure legends). Although the spectral differences between the two sets are clearly shown in the plots, one can expect ambiguities when the two parameters of disorder, L_a and L_D, come into play simultaneously in samples containing both 1D and 0D defects, as illustrated in figure 1(e). The reason is simple: two parameters of disorder (L_a and L_D) cannot be univocally extracted from one spectral information (A_D/A_G). Indeed, the plots shown in figures 1(c) and (d) are based on the assumptions $L_a \rightarrow \infty$, and $L_D \rightarrow \infty$, respectively. However, none of these two assumptions apply for samples containing both 1D and 0D defects. Therefore, to disentangle the information about point and line defects in such a system, a second different spectral information has to be taken into account. In the next section, we show that the G-band line width, Γ_G, serves the purpose.

3. The Raman diagram

Figure 2(a) shows the plot of A_D/A_G as a function Γ_G. Actually, A_D/A_G is multiplied by the fourth power of the excitation laser energy (E_L^4) in order to compare results obtained using different laser energies, once it has already been established that the A_D/A_G ratio scales with E_L^{-4} [14, 17, 24]. Filled symbols stand for samples with point defects (set 1) and open symbols stand for samples with line defects (set 2), both obtained with different excitation laser lines (see figure legend). Exemplary spectra along the amorphization trajectories for samples with line and point defects can be found in appendix A. Figures 2(b) and (c) plot Γ_G and $(A_D/A_G)E_L^4$ separately, as a function of the structural parameters that define the sample degree of disorder, L_D for the sample with point-defects (as illustrated in figure 1(a)), and L_a for the sample with line-defects (as illustrated in figure 1(b)). It is clear that Γ_G and $(A_D/A_G)E_L^4$ follow different functions of L_D and L_a, depending on the defect dimensionality, except for the two extremes (L_a, $L_D \rightarrow 0, \infty$), where the values converge. Therefore, the two spectral features, A_D/A_G and Γ_G, which are precisely the features that have been broadly studied to quantify defects in graphitic materials [8–15, 17–21, 23, 24, 26–30], form a pair of variables that can be used to disentangle the contribution from point and line defects in the Raman spectra of samples where these two types of structural disorder are intermixed, as illustrated in

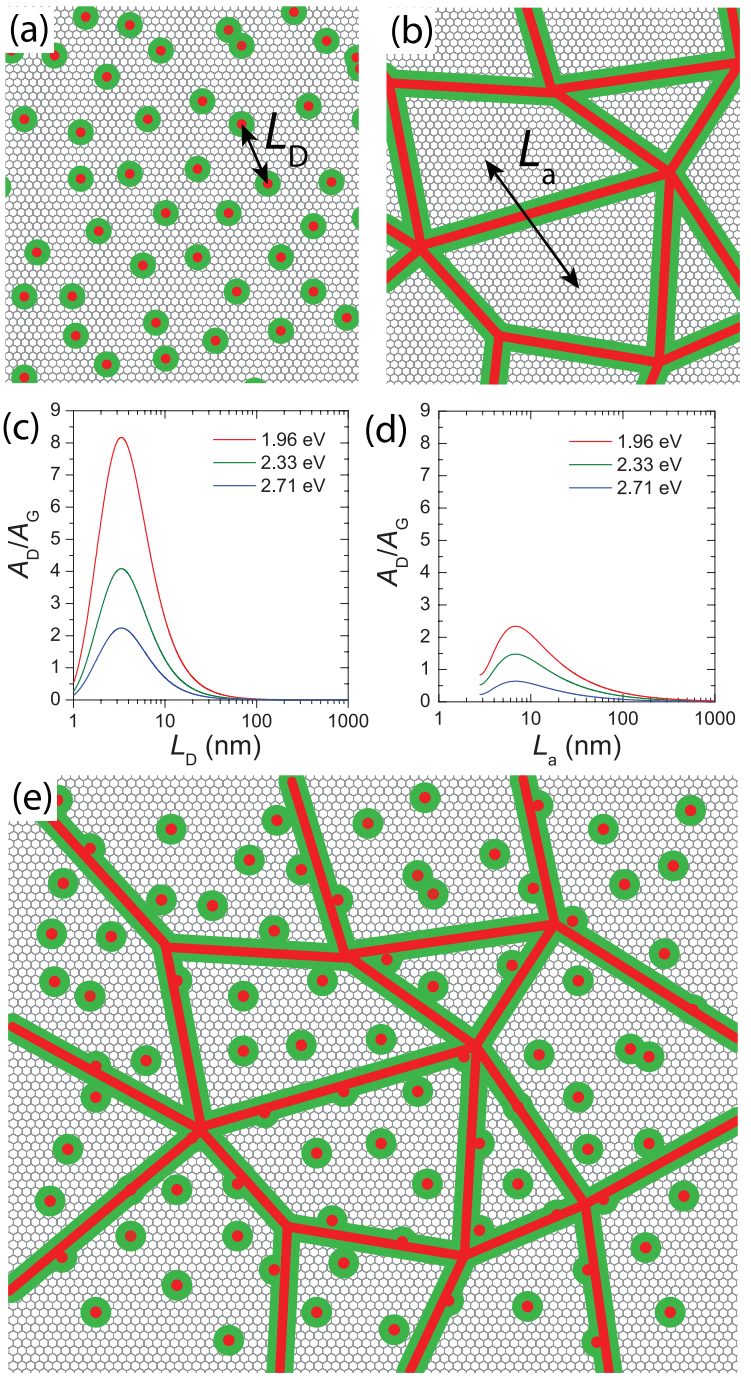

Figure 1. Illustrations of graphene samples with point defects (a), and line defects (b). ((c) and (d)) Theoretical plots of A_D/A_G as a function of L_D [19, 24] and L_a [14, 30], respectively, for three distinct values of excitation laser energies, E_L, as indicated in the legends. (e) Illustrations of a graphene sample containing both point and line defects. The red circles in ((a) and (e)) define the structurally-damaged area (*S*-region) surrounding a point defect [19]. These circles have radii r_S. The red lines in ((b) and (e)) are structurally-damaged ribbons (*S*-regions) of width l_S. The ribbons define the borders of crystallites in polycrystalline graphene [30]. The green circles and lines in ((a), (b) and (e)) are activated area (*A*-regions) surrounding structural defects where the D band is active [19, 30]. The extents of these A-regions (radii of circles or widths of lines) are defined by the electron coherence length ℓ_e [19, 22, 30].

figure 1(e). In this sense, the plot presented in figure 2(a) can be referred as a Raman diagram for graphene.

3.1. Definition of the relevant parameters

Lines and down-triangles in figure 2 are results from the theoretical modeling that explains how to build the Raman diagram. Modeling the amorphization routes shown in figure 2 requires the definition of the parameters ruling the inelastic light scattering process via phonons in graphene:

- Structural parameters: *point-defects*—r_S is the radius of the structurally-damaged area (*S*-region, illustrated as red circles in figures 1(a) and (e))

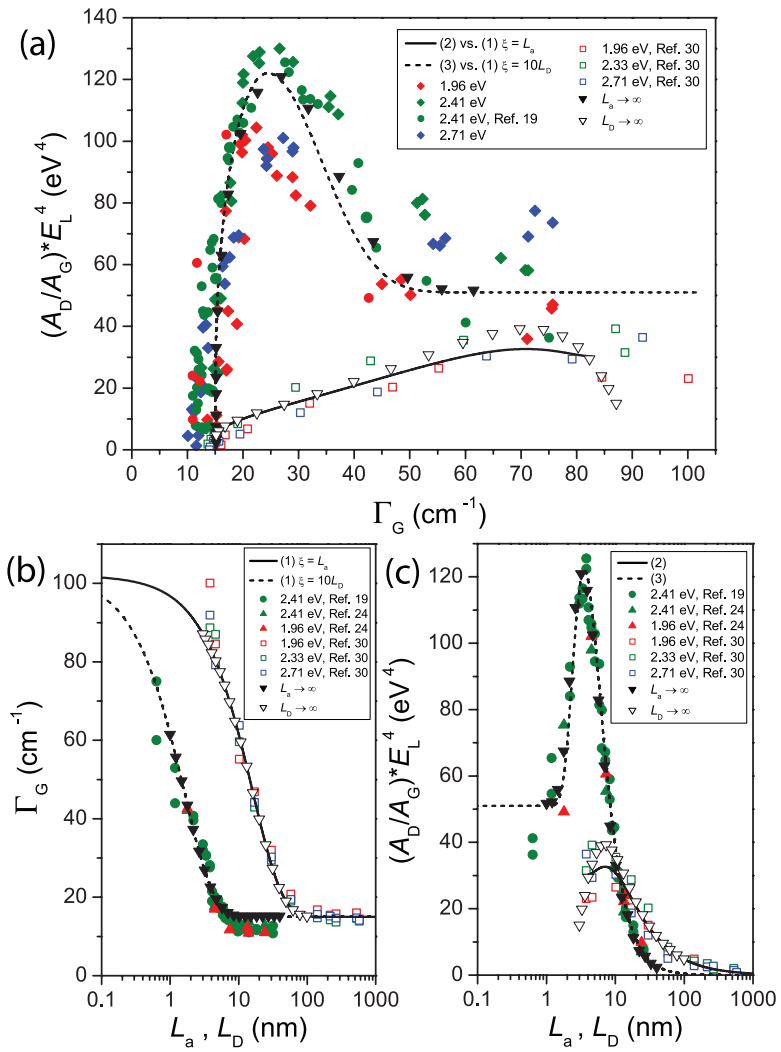

Figure 2. Spectral behavior for the amorphization routes in graphene materials. (a) $(A_D/A_G)E_L^4$ as a function of Γ_G. The solid line is a plot of the one-by-one correlation between the values obtained from equation (1) (with $\xi = L_a$) and (2), for L_a ranging from 4 to 1,000 nm in steps of 0.01 nm. Similarly, the dashed line correlates the values obtained from equation (1) (with $\xi = 10\ L_D$) and (3), for L_D ranging from 0.01 to 1,000 nm in steps of 0.01 nm. (b) Γ_G as a function of L_a and L_D, separately. The solid and dashed lines are the plots of equation (1) as a function of L_a ($\xi = L_a$) and L_D ($\xi = 10\ L_D$), respectively. (c) $(A_D/A_G)E_L^4$ as a function of L_a and L_D, separately. The solid and dashed lines are the plots of equations (2) and (3) as a function of L_a and L_D, respectively. In all panels, filled and open symbols represent samples with point- and line-defects, respectively. Same definition for dashed and solid lines, respectively. The value of E_L for each experimental data set is displayed in the legends, in eV units. The data represented by diamonds in (a) were generated for this work. The bullets and open squares were extracted from [19] and [30] , respectively. The filled up-triangles were taken from [24]. The empty and filled down-triangles are data obtained from numerical simulation with $L_a \rightarrow \infty$ and $L_D \rightarrow \infty$, respectively. Exemplary Raman spectra can be found in appendix A.

around a point-like defect, important for L_D determination [19, 20]; *line-defects*—l_S is the width of the structurally-damaged ribbon (illustrated as red lines in figures 1(b) and (e)) near a crystallite border in a polycrystalline sample, important for L_a determination [30].

- Dynamical parameters: electron [19, 22] and phonon [30, 34–36] coherence lengths in graphene, labeled here as ℓ_e and ℓ_{ph}, respectively. These two quantities are important for the Raman linewidth broadening, due the combined effects of quantum confinement and the uncertainty principle, and also for the D to G intensity ratio, by defining the region surrounding a structural defect where the D band is active (*A*-region, illustrated as green areas (circles and lines) in figures 1(a), (b) and (e)) [19, 20, 30].
- Raman cross-section ratios: The differential Raman cross-section ratios between D and G bands are described by four coefficients (C_S^{0D}, C_S^{1D}, C_A^{0D} and C_A^{1D}), taking into account the contributions to the D and G bands from either the *S*− or *A*−regions, for either point (0D) or line (1D) defects.

The G band linewidth (Γ_G) increases exponentially as the phonon localization length ξ decreases with respect to the phonon coherence length ℓ_{ph}, as proposed by Ribeiro-Soares *et al* [30]:

$$\Gamma_G(L_a, L_D) = \Gamma_G(\infty) + C_\Gamma\, e^{-\xi/\ell_{ph}}. \qquad (1)$$

For samples with only line defects $\xi = L_a$ (since phonons are confined within a crystallite of size L_a), while for samples with pure point defects $\xi = \alpha L_D$. It will be shown that $\alpha > 1$, which is expected because point defects are less effective in localizing phonons when compared to line defects.

The $(A_D/A_G)E_L^4$ ratio for each sample is computed by summing contributions for the D and G bands from $S-$ and $A-$regions. $S-$regions are either circles of radius r_S at each point defect, or ribbons of widths l_S at crystallite edges. These two regions define the area that contribute $C_S^{(0D,1D)} f_{S,(0D,1D)}$ to $(A_D/A_G)E_L^4$, where $f_{S,(0D,1D)}$ is the fraction of total sample area occupied by the $S-$region in (0D,1D) defects. In $A-$regions, contributions to $(A_D/A_G)E_L^4$ are calculated by assuming that the probability of D band scattering decreases exponentially with the distance from the $S-$region (see appendix B), with decay length ℓ_e (electron coherence length) [22, 30].

3.2. Simulations

Next, we determine all these parameters from simulations for the reference cases of samples with only point defects or samples with only line defects, and use them to predict the behavior of the more general case of samples containing both kinds of defects.

3.2.1. *Simulations for samples with line defects*

In this case, for a given average crystallite size $\overline{L}_a$, we take an ensemble of 20 square crystallites with sizes L_a randomly chosen from a Gaussian distribution centered at $\overline{L}_a$, and with a standard deviation of $\overline{L}_a/4$. This is roughly the width of crystallite size distributions of polycrystalline graphite [30]. The G band linewidth for each crystallite is calculated using equation (1), with $\xi = L_a$. In figure 2(b), our simulation results (open down-triangles) are plotted together with experimental data (see legend and caption). We find that $\ell_{ph} = 16$ nm, $C_\Gamma = 87\ \mathrm{cm}^{-1}$ and $\Gamma_G(\infty) = 15 \times 10^{12}\ \mathrm{s}^{-1}$ fit well the experimental data (these parameters are summarized in table 1). The analytical expression $\Gamma_G(\overline{L}_a)$ obtained simply by substituting L_a by the average value $\overline{L}_a$ in equation (1) also fits the experimental data satisfactorily (solid line in figure 2(b)).

The open triangles in figure 2(c) are results from simulations for $(A_D/A_G)E_L^4$, obtained with the parameters $C_S^{1D} = 30.3\ \mathrm{eV}^4$, $C_A^{1D} = 30.4\ \mathrm{eV}^4$, $l_S = 2.0$ nm and $\ell_e = 4.1$ nm (these parameters are summarized in table 1). An analytical approximation to the simulation data can be obtained (see appendix B), and it is given by

$$\left(\frac{A_D}{A_G}\right)E_L^4(\overline{L}_a) = \frac{1}{\overline{L}_a^2}\left[4C_S^{1D} l_S(\overline{L}_a - l_S) + 2C_A^{1D}\ell_e(\overline{L}_a - 2l_S) \times \left(1 - e^{-\frac{\overline{L}_a - 2l_S}{\ell_e}}\right)\right]. \quad (2)$$

Table 1. Numerical values (central column) for the fitting parameters found in this work (left column), after fitting experimental data with the proposed equations (indicated in the last column).

Parameter	Value (unit)	Equation
C_Γ	$87\ \mathrm{cm}^{-1}$	(1)
$\Gamma_G(\infty)$	$15\ \mathrm{cm}^{-1}$	(1)
ℓ_{ph}	16 nm	(1)
C_S^{1D}	$30.3\ \mathrm{eV}^4$	(2) and (4)
C_A^{1D}	$30.4\ \mathrm{eV}^4$	(2) and (4)
ℓ_e	4.1 nm	(2) and (4)
l_S	2 nm	(2) and (4)
ℓ_e	3.7 nm	(3)
C_S^{0D}	$51\ \mathrm{eV}^4$	(3) and (4)
C_A^{0D}	$26.5\ \mathrm{eV}^4$	(3) and (4)
r_S	2.2 nm	(3)

This analytical function fits both experimental and simulation data, as shown by the solid line in figure 2(c).

3.2.2. *Simulations for samples with point defects*

In this case, we consider borderless graphene with periodic boundary conditions and a target point defect concentration σ, which defines the average distance between defects $\overline{L}_D$ as $\sigma = 1/\overline{L}_D^2$. We consider 20 realizations of random defect distributions for each value of $\overline{L}_D$. The G band linewidth for a given L_D is given by equation (1), with $\xi = \alpha L_D$. We find that $\alpha = 10$ reproduces the experimental data, showing that point-defect disorder leads to G band phonon localization lengths that are approximately 10 times larger than the average distance between defects. This is consistent with calculated localization lengths for K-point phonons in graphene with a disordered distribution of vacancies [37]. The remaining parameters ($\Gamma_G(\infty)$, C_Γ and ℓ_{ph}) are the same as in the case of line defects. Simulation data are the filled down-triangles in figure 2(b), and once again an analytical approximation given by the substitution of L_D by the average value $\overline{L}_D$ in equation (1) fits well the experimental data (dashed line in figure 2(b)).

For computing the $(A_D/A_G)E_L^4$ ratio, $S-$regions are now randomly-distributed disks of radii r_S which may overlap each other. Results from the simulations are indicated by filled down-triangles in figure 2(c), obtained with parameters $C_S^{0D} = 51\ \mathrm{eV}^4$, $C_A^{0D} = 26.5\ \mathrm{eV}^4$, $r_S = 2.2$ nm and $\ell_e = 3.7$ nm (these parameters are summarized in table 1). Notice that the values of ℓ_e obtained by fitting the experimental data for samples with line and point defects are quite similar, which gives us confidence to associate them with the same physical quantity (electron coherence length) [19, 22, 30].

Again, an analytical approximation to the simulation data can be obtained by solving the rate equations for the evolution of $S-$ and $A-$regions, in a similar manner to [19]. The resulting equation is

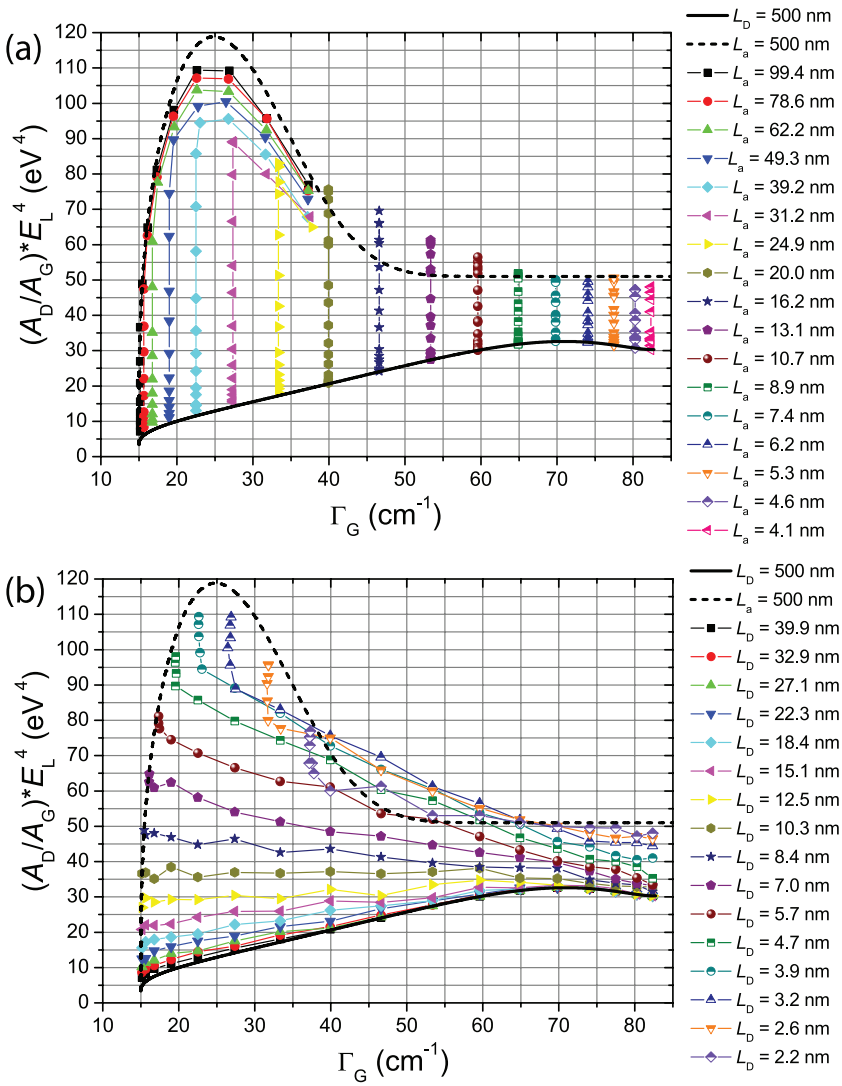

Figure 3. Theoretical calculation for the $(A_D/A_G)E_L^4$ as a function of the G band spectral linewidth Γ_G. The symbols were obtained from numerical simulations (see text). In (a), equal symbols connected by lines represent samples with a given L_a value (indicated in the legend), with decreasing L_D distances from smaller to larger Γ_G values. (b) The opposite: equal symbols connected by lines represent samples with a given L_D value (indicated in the legend), with decreasing L_a distances from smaller to larger Γ_G values. The dashed lines in (a) and (b) are the same plot of $(A_D/A_G)E_L^4$ as a function of Γ_G obtained from equations (4) and (1), respectively, by varying L_D and considering a fixed value of $L_a = 500$ nm. The solid lines correlate $(A_D/A_G)E_L^4$ with Γ_G (obtained from equations (4) and (1), respectively) for different values of L_a, with L_D fixed at 500 nm.

$$\left(\frac{A_D}{A_G}\right)E_L^4(\overline{L}_D) = C_S^{0D}\left(1 - e^{-\frac{\pi r_S^2}{\overline{L}_D^2}}\right) + \frac{2\pi}{\overline{L}_D^2}C_A^{0D}\ell_e(\ell_e + r_S)e^{-\frac{\pi r_S^2}{\overline{L}_D^2}}, \quad (3)$$

which is displayed in dashed lines in figure 2(c).

3.2.3. *Simulations for samples with point and line defects*

With parameters obtained from the simulations for the reference cases of purely point or line defects, simulations in which both kinds of defects are present simultaneously can be performed. The resulting Γ_G and $(A_D/A_G)E_L^4$ are then functions of both L_a and L_D (from now on we drop the overline symbol that indicates average). We map both functions in a dense grid of 20 × 20 values of $L_a \times L_D$. For each pair (L_a, L_D), 20 realizations of disorder are considered and average values for both Γ_G and $(A_D/A_G)E_L^4$ are calculated.

Since now both crystallite size and point defects contribute to phonon localization, the localization length ξ is chosen as the minimum value between L_a and αL_D. Determination of $(A_D/A_G)E_L^4$ proceeds as before, by considering a random distribution of disks, but now for crystallites of finite size L_a. The results are summarized in figure 3. Both top and bottom panels show the same Γ_G versus $(A_D/A_G)E_L^4$ data, but organized in different manner, as described in the caption. The same symbol is used for samples with a fixed value of L_a (panel (a)) or L_D (panel (b)) (values displayed in the legends, in nm units).

Once again, an analytical approximation to the $(A_D/A_G)E_L^4$ simulation data can be obtained by solving the approximate rate equations for evolution of $S-$ and $A-$regions, as described in detail in appendix C, resulting in the following equation:

$$\left(\frac{A_D}{A_G}\right)E_L^4(L_a, L_D) = C_S^{0D}\left(1 - e^{-\frac{\pi r_S^2}{L_D^2}}\right) + 4C_S^{1D} l_S \frac{(L_a - l_S)}{L_a^2} e^{-\frac{\pi r_S^2}{L_D^2}} + 2\pi C_A^{0D} \ell_e \frac{(\ell_e + r_S)}{L_D^2}\left[1 - 4l_S\frac{(L_a - l_S)}{L_a^2}\right] e^{-\frac{\pi r_S^2}{L_D^2}} + 2C_A^{1D}\ell_e \frac{(L_a - 2l_S)}{L_a^2}\left(1 - e^{-\frac{L_a - 2l_S}{\ell_e}}\right) e^{-\frac{\pi r_S^2}{L_D^2}}, \quad (4)$$

with all numerical parameters, which were found in this work, summarized in table 1.

The dashed lines in figures 3(a) and (b) are the plot of $(A_D/A_G)E_L^4$ as a function of Γ_G obtained from equations (4) and (1), respectively, by varying L_D and considering a fixed value of $L_a = 500$ nm. This curve falls in the limit $L_a \gg \ell_e$, which reproduces $L_a \to \infty$ (pure point defects). Similarly, the solid lines in figures 3(a) and (b) correlate $(A_D/A_G)E_L^4$ with Γ_G (obtained from equations (4) and (1), respectively) for different values of L_a, with L_D fixed at 500 nm ($L_D \gg \ell_e$, reproducing pure line defects). These two curves delimit a phase space that embraces samples with 0D and 1D defects, and the plots in figure 3 provide a user-friendly diagram for the defects quantification.

Notice that, in the largest portion of the Raman diagram shown in figure 3, a given point $[\Gamma_G, (A_D/A_G)E_L^4]$ determines unambiguously the pair (L_a, L_D) and therefore allows disentanglement of the contributions from point and line defects, fully based on the D and G Raman spectral information. However, in small parts of the Raman diagram, where different line trajectories cross, there is ambiguity in defining (L_a, L_D) and the disentanglement is not possible.

In addition, researchers have to be careful when using figure 3 and related equations for estimating the concentrations of point and line defects in the extreme-left side of the diagram. Within this region, Γ_G changes between 15 and 20 cm^{-1} for L_a between infinity and 45 nm, or L_D between infinity and 4.5 nm. Definitive (L_a, L_D) assignments are not accurate here because Γ_G changes within this range also because of strain, doping, and number of layers [38, 39]. At this extreme, the Tuinstra–Koenig\Cançado relation [8, 14], $(A_D/A_G) = (\mathbf{6}\ /E_L^4)/L_a$ (L_a in nm units), still broadly used to quantify defects in graphene, is valid for 1D defects, which is on top of the solid lines in figures 2(a) and 3(a) and (b), from the lowest value of Γ_G up to $\Gamma_G \sim 20$ cm^{-1}. For $L_a <$ 0 nm, or in the presence of point defects, the Tuinstra–Koenig\Cançado relation is not valid. For samples with only point defects, another simple relation was introduced in [19, 24], which is $(A_D/A_G) = (4300/E_L^4)/L_D^2$ (L_D in nm units). This relation is also restricted, valid only on top of the dashed line in figures 2(a) and 3(a), (b), from the lowest value of Γ_G up to $\Gamma_G \sim 20$ cm^{-1} as well. This is equivalent to graphene with average distance among defects down to $L_D \sim 4.5$ nm. For $L_D < 4.5$ nm or in the presence of line defects, the relation is not valid either. For samples with $L_D > 4.5$ nm and/or $L_a > 45$ nm, accurate disentanglement of point and line defects requires systematic work for addressing the effects of doping, strain and the number of layers in the relevant spectral parameters. For samples outside these limited ranges, figure 3 and the related equations can be used to quantify and identify defect dimensionality.

4. Application of the method

An example of how the methodology developed here can enhance significantly the importance of using Raman spectroscopy to characterize graphene-related technologies is given now. Hof *et al* [40] reported the production of graphitic nanoparticles from a sustainable carbon feedstock for ink and conductive coating applications. This work is specifically interesting to be analyzed here, not only because of its technological importance, but also because it brings an extensive characterization of their samples, performed with different techniques. More specifically, five different samples were produced by the cracking of methane/CO_2 mixtures into graphitic carbon and hydrogen, via the cold microwave plasma method, by setting different initial CO_2 contents, namely 0% (NC_0), 0.4% (NC_1), 1.7% (NC_2), 4.9% (NC_3) and 7.4% (NC_4). The synthesis was followed by a controlled heat-treatment at 500° C for 6 h, for sample purification [40]. Besides Raman spectroscopy, the authors performed resistivity measurements, and demonstrated that the lower average resistivity of the films produced from these nanocarbon materials was obtained for NC_2, followed by NC_1. They also performed thermogravimetric analysis, showing that the mass loss was minimized for NC_1, followed by NC_2. X-ray diffraction experiments indicated the highest crystallinity for NC_1, followed by NC_0 and then NC_2. Sample NC_4 exhibited the highest average volume resistance, highest mass loss, and lowest crystallinity.

Figure 4(a) shows the Raman diagram (plot of the $(A_D/A_G)E_L^4$ as a function of Γ_G) extracted from the Raman spectra of the as-grown NC samples. The data points are average values extracted from 1681 spectra taken from different regions in each sample, and our results are fully consistent with the Raman results reported in [40], where one can find exemplary Raman spectra. The effect of changing the CO_2 contents can be better understood by transforming the $((A_D/A_G)E_L^4, \Gamma_G)$ data of figure 4(a) into the plot of defect density ($\sigma = 1/L_D^2$) versus crystallite area (L_a^2), shown in figure 4(b), where the respective (L_a, L_D) values are extracted from figure 3. The samples occupy different positions on the 0D versus 1D defect diagram, and this information can be used to get insights into the quality of the resulting material. Sample NC_4 is

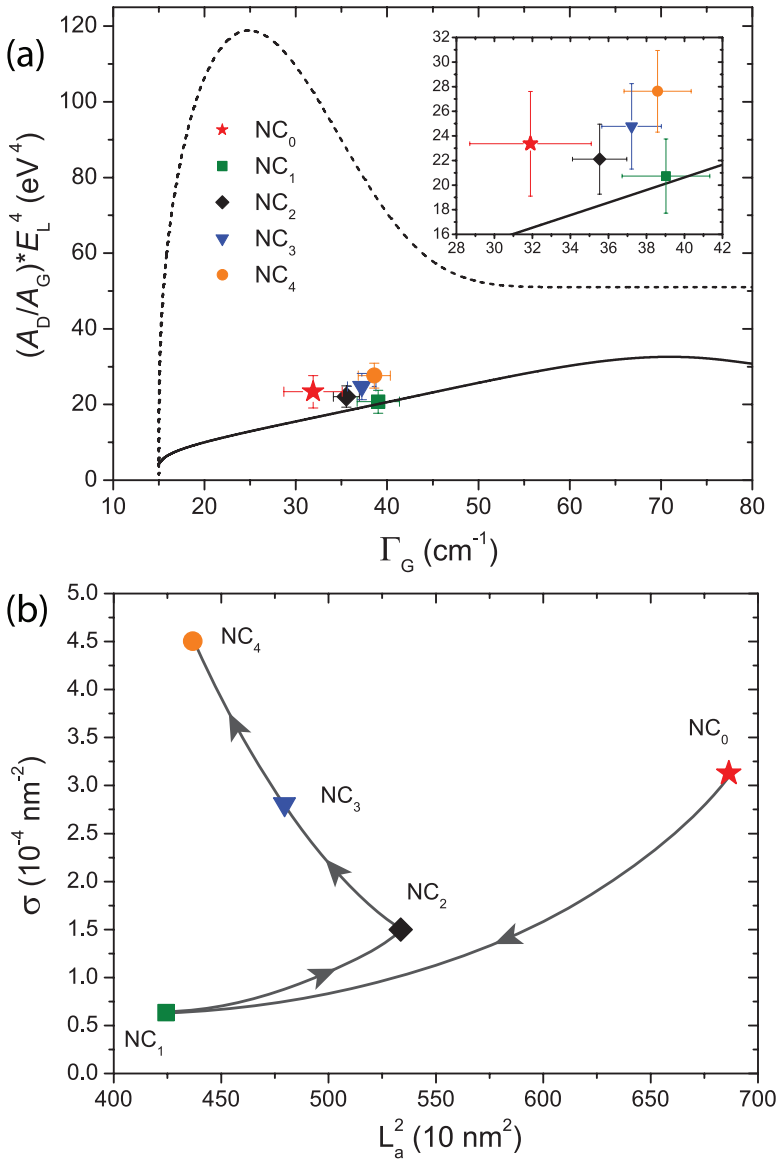

Figure 4. Characterization of graphene-related samples produced by the cracking of a methane/CO_2 mixture into graphitic carbon and hydrogen via the cold microwave plasma method. [40] The five distinct samples were produced by setting different initial CO_2 contents, namely 0% (NC_0), 0.4% (NC_1), 1.7% (NC_2), 4.9% (NC_3) and 7.4% (NC_4).(a) $(A_D/A_G)E_L^4$ as a function of Γ_G. Data points correspond to average values extracted from 1681 spectra taken from different regions in each sample. The lengths of the error bars resemble the standard deviation. The solid and dashed lines are the same as in figure 3, reproduced here for reference. The inset is a zoom within the experimental data. (b) Plot of the defect density ($\sigma = 1/L_D^2$) versus crystallite area (L_a^2), with the respective (L_a, L_D) values are extracted from figure 3. Exemplary Raman spectra can be found in [40].

the most defective, exhibiting the worse compromise between density of point defects (highest) and crystallite size (lowest). This is in agreement with the results reported by Hof *et al* [40]. With respect to crystallinity, sample NC_0 appears as being superior to NC_2 and NC_3, and this is not because the density of point defects is small, but because the crystallite sizes for the samples obtained without the CO_2 additive are considerably higher than the ones obtained with the CO_2 additive. The mass loss observed by Hof *et al* [40] scales very nicely with the density of point defects. Finally, the average volume resistivity is observed to be best for sample NC_2, which shows the best compromise between lower amount of defects and larger crystallite sizes, i.e. the best compromise on minimizing the amount of one and two-dimensional defects together. On this sense, the Raman diagram shown in figure 4(b) suggests that a fine tunning should be performed with samples where the CO_2 additive varies between 0% (NC_0) and 1.7% (NC_2), trying to populate the low-right quadrant of the Raman diagram in figure 4(b).

5. Conclusions

In summary, figure 3 and the related equations contain clear specifications for the quantification of defects, establishing a protocol for disentangling the contributions of point-like and line-like defects to the Raman spectra of

2D sp^2 carbon materials. It can be useful for understanding and optimizing processes of synthesis, purification, and functionalization, where both L_a and L_D can change, as demonstrated here for graphitic nanocarbon made for inks and conductive coatings. L_a and L_D appear as the significant structural parameters that rule transition between perfect graphene to amorphous carbon, and figure 3 can be used to identify their values.

Acknowledgments

The Authors acknowledge the financial support from CNPq (grants 307067/2015-7, 460045/2014-8 and 552124/2011-7), CAPES, FAPEMIG, FAPERJ, INCT-Nanomateriais de Carbono and Inmetro. Funding from the European Union's Seventh Framework Program for research, technological development and demonstration under grant agreement No 603488 (Plascarb project) is acknowledged.

Appendix A. Exemplary Raman spectra along the amorphization trajectory for samples with line and point defects

Figure A1 shows exemplary spectra within the Raman phase diagram of figure 2(a), following the amorphization routes with only line or only point defects (see figure legend). From figure A1, one has a good feeling of the spectral changes in (A_D/A_G) and Γ_G within the Raman phase diagram.

Appendix B. Calculation of $(A_D/A_G)\,E_L^4$ for a single crystallite without point defects

The $(A_D/A_G)E_L^4$ ratio for a single crystallite is computed by summing contributions from $S-$ and $A-$regions. $S-$regions are ribbons of width l_S at crystallite edges and they contribute $C_S^{1D} f_{S,1D}$ to $(A_D/A_G)E_L^4$, where $f_{S,1D}$ is the fraction of total crystallite area occupied by the $S-$region:

$$f_{S,D} = \frac{4l_S(L_a - l_S)}{L_a^2}. \tag{B.1}$$

In $A-$regions, contributions to $(A_D/A_G)E_L^4$ are calculated by assuming that the probability of D band scattering decreases exponentially with the distance from the $S-$region, with decay length ℓ_e (electron coherence length) [30]. Polarization effects are taken into account by considering electric fields polarized along y, which means that only distances from the left and right vertical $S-$region ribbons are relevant [30]. The contribution to $(A_D/A_G)E_L^4$ from a square crystallite of size L_a is then given by:

$$\left(\frac{A_D}{A_G}\right)E_L^4(L_a) = C_S^{1D} f_{S,1D} + \frac{1}{L_a^2}\int_A C_A^{1D}\left(e^{-\frac{|x-l_S|}{\ell_e}} + e^{-\frac{|L_a-l_S-x|}{\ell_e}}\right)dA, \tag{B.2}$$

where x is the horizontal coordinate of a point inside the crystallite and the integral is taken over the A-region (which is the whole crystallite except the S-region).

The analytical approximation given in equation (2) of the main text is obtained by substituting L_a for the average value $\overline{L}_a$ and performing the integration in equation (B.2).

Appendix C. Calculation of $(A_D/A_G)\,E_L^4$ for single crystallites with point defects

We start our analysis with the assumption that the $(A_D/A_G)E_L^4$ intensity ratio is composed by the sum of three contributions

$$\left(\frac{A_D}{A_G}\right)E_L^4 = \left(\frac{A_D}{A_G}\right)_{0D}^{(S)} + \left(\frac{A_D}{A_G}\right)_{1D}^{(S)} + \left(\frac{A_D}{A_G}\right)_{0D,1D}^{(A)}, \tag{C.1}$$

where $(A_D/A_G)_{0D}^{(S)}$ is the contribution from S-regions around point defects, $(A_D/A_G)_{1D}^{(S)}$ is the contribution from S-regions near borders, and $(A_D/A_G)_{0D,1D}^{(A)}$ is the contribution from A-regions (including activation due to both, point defects and borders).

C.1. Calculation of $(A_D/A_G)_{0D}^{(S)}$

This is exactly the same as in the case of an infinite graphene sheet [19]

$$\left(\frac{A_D}{A_G}\right)_{0D}^{(S)} = C_S^{0D} f_{S,0D}(\sigma), \tag{C.2}$$

where $f_{S,0D}(\sigma)$ is the fraction of the total area occupied by point-defect S-regions

$$f_{S,0D}(\sigma) = 1 - e^{-\pi r_S^2 \sigma}, \tag{C.3}$$

with $\sigma = 1/L_D^2$ being the defect density.

C.2. Calculation of $(A_D/A_G)_{1D}^{(S)}$

If a point defect is located near a border, it will remove some of the border's contribution to the overall D band intensity. In this case, $(A_D/A_G)_{1D}^{(S)}$ will be a function of σ on the form

$$\left(\frac{A_D}{A_G}\right)_{1D}^{(S)} = C_S^{1D} f_{S,1D}(\sigma), \tag{C.4}$$

where $f_{S,1D}(\sigma)$ is the ratio between the S-region near the borders (A_B), and the total area A_T, which is

$$f_{S,1D}(\sigma) = \frac{A_B}{A_T}. \tag{C.5}$$

The σ-dependency of $f_{S,1D}(\sigma)$ comes from the fact that each point defect near a border removes an area πr_S^2 from the A_B area generating D band scattering, that is

$$\frac{dA_B}{dN} = -\pi r_S^2 \frac{A_B}{A_T}, \tag{C.6}$$

with N being the total number of point defects. This equation can be readily integrated to give

$$A_B(\sigma) = A_B(0)e^{-\pi r_S^2 \sigma}, \tag{C.7}$$

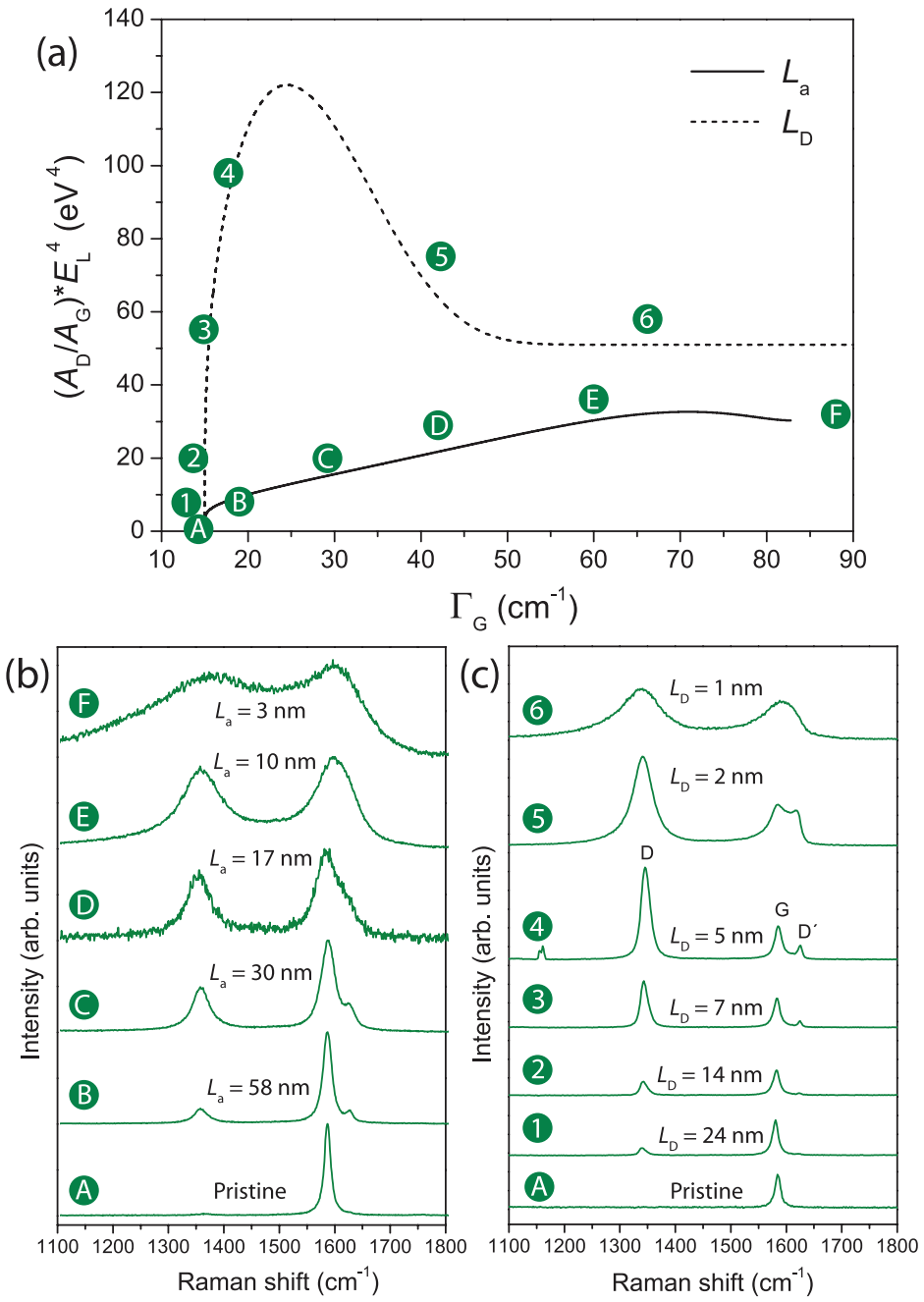

Figure A1. Exemplary Raman spectra within the Raman phase diagram of figure 2. (a) Reproduces the $(A_D/A_G)E_L^4$ as a function of Γ_G theoretical diagram (lines), showing only the experimental data points related to the Raman spectra shown in (b) and (c). (b) Exemplary Raman spectra for samples following the amorphization route of pure line defects. (c) Exemplary Raman spectra for samples following the amorphization route of pure point defects. The letters/numbers correlate the specific spectrum in (b)/(c) with the spectral location at the Raman phase diagram in (a).

where we have used $\sigma = N/A_T$. Dividing both sides of equation (C.7) by A_T yields

$$f_{S,1D}(\sigma) = f_{S,1D}(0)e^{-\pi r_S^2 \sigma}. \quad (C.8)$$

We now recall that $f_{S,1D}(0)$ is the initial value of $f_{S,1D}$, where no point defects are present (equation (B.1)). As a final step, equations (B.1) and (C.8) can be inserted into equation (C.4), which assumes the form

$$\left(\frac{A_D}{A_G}\right)_{1D}^{(S)} = C_S^{1D}\frac{4l_S(L_a - l_S)}{L_a^2}e^{-\pi r_S^2\sigma}. \quad (C.9)$$

C.3. Calculation of $(A_D/A_G)_{0D,1D}^{(A)}$

We start our analysis by considering the quantity $\Delta_{0D,1D}^{(A)}$, the contribution to $(A_D/A_G)_{0D,1D}^{(A)}$ from a single point defect:

$$\Delta_{0D,1D}^{(A)} = C_A^{0D}\int_{r_S}^{r_c} 2\pi r e^{-(r-r_S)/\ell_e}dr \quad (C.10)$$

Here, the cutoff radius r_c is determined by the condition that the area of integration is the same for a circular region and a square cluster of side $L_a - 2l_S$, that is

$$\pi r_c^2 = (L_a - 2l_S)^2. \quad (C.11)$$

Back to equation (C.10), the integration yields

$$\Delta^{(A)}_{0D,1D} = 2\pi C_A^{0D}\ell_e\left[\ell_e + r_S - (\ell_e + r_c)e^{-(r_c - g)/\ell_e}\right]. \quad (C.12)$$

The rate equation for $(A_D/A_G)^{(A)}_{0D,1D}$ is

$$\frac{d}{dN}\left(\frac{A_D}{A_G}\right)^{(A)}_{\mathbb{D},1D} = \left[\Delta^{(A)}_{\mathbb{D},1D}[1 - f_S(\sigma) - f_{S,1D}(\sigma)] - \pi r_S^2\left(\frac{A_D}{A_G}\right)^{(A)}_{\mathbb{D},1D}\right]\frac{1}{A_T}. \quad (C.13)$$

While the first term considers the increase of activation in the A-region, the second accounts for the decrease in activation due to the increase of S-regions. Next, we use $\sigma = N/A_T$, $f_S(\sigma) = 1 - e^{-\pi r_S^2\sigma}$ (equation (C.3)), and $f_{S,1D}(\sigma) = f_{S,1D}(0)e^{-\pi r_S^2\sigma}$ (equation (C.8)) to rewrite (C.13) in the form:

$$\frac{d}{dN}\left(\frac{A_D}{A_G}\right)^{(A)}_{0D,1D} = \Delta^{(A)}_{0D,1D}e^{-\pi r_S^2\sigma}[1 - f_{S,1D}(0)] - \pi r_S^2\left(\frac{A_D}{A_G}\right)^{(A)}_{0D,1D}. \quad (C.14)$$

We propose a solution to (C.14) of the type

$$\left(\frac{A_D}{A_G}\right)^{(A)}_{0D,1D} = \left(\frac{A_D}{A_G}\right)_\sigma e^{-\pi r_S^2\sigma}, \quad (C.15)$$

and we find the following rate equation for $(A_D/A_G)_\sigma$:

$$\frac{d}{d\sigma}\left(\frac{A_D}{A_G}\right)_\sigma = \Delta^{(A)}_{\mathbb{D},1D}[1 - f_{S,\mathbb{D}}(\sigma)], \quad (C.16)$$

with the general a solution

$$\left(\frac{A_D}{A_G}\right)_\sigma = \Delta^{(A)}_{0D,1D}[1 - f_{S,1D}(0)]\sigma + \beta. \quad (C.17)$$

β is a constant determined by the initial condition $\beta = (A_D/A_G)_0 = (A_D/A_G)(L_a)$, with $(A_D/A_G)(L_a)$ being the D band intensity for samples with borders only (no point defects). This quantity has been calculated before (second term at the right-hand side of equation (B.2)), and has the form

$$\left(\frac{A_D}{A_G}\right)(L_a) = 2C_A^{1D}\frac{\ell_e}{L_a^2}(L_a - 2l_S)[1 - e^{-(L_a - 2l_S)/\ell_e}]. \quad (C.18)$$

We can finally group and substitute equations (B.1), (C.12), (C.17) and (C.18) into equation (C.15) to have

$$\left(\frac{A_D}{A_G}\right)^{(A)}_{0D,1D} = 2\pi C_A^{0D}\ell_e\frac{(\ell_e + r_S)}{L_D^2}\left[1 - 4l_S\frac{(L_a - l_S)}{L_a^2}\right]e^{-\frac{\pi r_S^2}{L_D^2}} + 2C_A^{1D}\ell_e\frac{(L_a - 2l_S)}{L_a^2}\left(1 - e^{-\frac{L_a - 2l_S}{\ell_e}}\right)e^{-\frac{\pi r_S^2}{L_D^2}}. \quad (C.19)$$

References

[1] Banhart F, Kotakoski J and Krasheninnikov A V 2010 *ACS Nano* **5** 26
[2] Yazyev O V and Chen Y P 2014 *Nat. Nanotechnol.* **9** 755
[3] Vicarelli L, Heerema S J, Dekker C and Zandbergen H W 2015 *ACS Nano* **9** 3428
[4] Zhao W, Wang Y, Wu Z, Wang W, Bi K, Liang Z, Yang J, Chen Y, Xu Z and Ni Z 2015 *Sci. Rep.* **5** 11962
[5] Song J C, Reizer M Y and Levitov L S 2012 *Phys. Rev. Lett.* **109** 106602
[6] López-Polín G, Gómez-Navarro C, Parente V, Guinea F, Katsnelson M, Pérez-Murano F and Gómez-Herrero J 2015 *Nat. Phys.* **11** 26
[7] Koepke J C, Wood J D, Estrada D, Ong Z Y, He K T, Pop E and Lyding J W 2013 *ACS Nano* **7** 75
[8] Tuinstra F and Koenig J L 1970 *J. Chem. Phys.* **53** 1126
[9] Dresselhaus M S, Dresselhaus G, Sugihara K, Spain I L and Goldberg H A 2013 *Graphite Fibers and Filaments* vol 5 (Berlin: Springer)
[10] Dresselhaus M S and Kalish R 2013 *Ion Implantation in Diamond, Graphite and Related Materials* vol 22 (Berlin: Springer)
[11] Ferrari A and Robertson J 2000 *Phys. Rev.* B **61** 14095
[12] Takai K, Oga M, Sato H, Enoki T, Ohki Y, Taomoto A, Suenaga K and Iijima S 2003 *Phys. Rev.* B **67** 214202
[13] Ferrari A and Robertson J 2004 *Phil. Trans. R. Soc.* A **362** 2477
[14] Cançado L G, Takai K, Enoki T, Endo M, Kim Y A, Mizusaki H, Jorio A, Coelho L N, Magalhes Paniago R and Pimenta M A 2006 *Appl. Phys. Lett.* **88** 163106
[15] Ferrari A 2007 *Solid State Commun.* **143** 47
[16] Casiraghi C, Hartschuh A, Qian H, Piscanec S, Georgi C, Fasoli A, Novoselov K, Basko D and Ferrari A 2009 *Nano Lett.* **9** 1433
[17] Pimenta M A, Dresselhaus G, Dresselhaus M S, Cancado L G, Jorio A and Saito R 2007 *Phys. Chem. Chem. Phys.* **9** 1276
[18] Dresselhaus M S, Jorio A, Hofmann M, Dresselhaus G and Saito R 2010 *Nano Lett.* **10** 751
[19] Lucchese M M, Stavale F, Ferreira E H M, Vilani C, Moutinho M V O, Capaz R B, Achete C A and Jorio A 2010 *Carbon* **48** 1592
[20] Ferreira E M, Moutinho M V, Stavale F, Lucchese M, Capaz R B, Achete C and Jorio A 2010 *Phys. Rev.* B **82** 125429
[21] Jorio A, Lucchese M M, Stavale F, Ferreira E H M, Moutinho M V, Capaz R B and Achete C A 2010 *J. Phys.: Condens. Matter.* **22** 334204
[22] Beams R, Cançado L G and Novotny L 2011 *Nano Lett.* **11** 1177
[23] Jorio A, Dresselhaus M, Ricchiro S and Dresselhaus G 2011 *Raman Spectroscopy in Graphene Related Systems* (Weinheim: Wiley)
[24] Cançado L, Jorio A, Ferreira E M, Stavale F, Achete C, Capaz R, Moutinho M, Lombardo A, Kulmala T and Ferrari A 2011 *Nano Lett.* **11** 3190
[25] Eckmann A, Felten A, Mishchenko A, Britnell L, Krupke R, Novoselov K S and Casiraghi C 2012 *Nano Lett.* **12** 3925
[26] Jorio A 2012 *ISRN Nanotechnol.* **2012**
[27] Jorio A and Cançado L G 2012 *Phys. Chem. Chem. Phys.* **14** 15246
[28] Jorio A, Ribeiro-Soares J, Cançado L, Falcao N, Dos Santos H, Baptista D, Ferreira E M, Archanjo B and Achete C 2012 *Soil Till. Res.* **122** 61
[29] Ribeiro-Soares J, Cançado L, Falcao N, Martins Ferreira E, Achete C and Jorio A 2013 *J. Raman Spectrosc.* **44** 283
[30] Ribeiro-Soares J *et al* 2015 *Carbon* **95** 646
[31] Beams R, Cançado L G and Novotny L 2015 *J. Phys.: Condens. Matter* **27** 083002
[32] Ahlberg P, Johansson F, Zhang Z B, Jansson U, Zhang S L, Lindblad A and Nyberg T 2016 *APL Mater.* **4** 046104
[33] Zeng J, Liu J, Yao H, Zhai P, Zhang S, Guo H, Hu P, Duan J, Mo D, Hou M and Sun Y M 2016 *Carbon* **100** 16

[34] Maximiano R V, Beams R, Novotny L, Jorio A and Cançado L G 2012 *Phys. Rev.* B **85** 235434
[35] Beams R, Cançado L G, Oh S H, Jorio A and Novotny L 2014 *Phys. Rev. Lett.* **113** 186101
[36] Cançado L G, Beams R, Jorio A and Novotny L 2014 *Phys. Rev.* X **4** 031054
[37] Islam M S, Rahaman M T, Bhuiyan A G and Hashimoto A 2015 *J. Circuits Syst. Comput.* **24** 1540002
[38] Shin Y, Lozada-Hidalgo M, Sambricio J L, Grigorieva I V, Geim A K and Casiraghi C 2016 *Appl. Phys. Lett.* **108** 221907
[39] Pisana S, Lazzeri M, Casiraghi C, Novoselov K S, Geim A K, Ferrari A C and Mauri F 2007 *Nat. Mater.* **6** 198
[40] Hof F, Kampioti K, Huang K, Jaillet C, Derré A, Poulin P, Yusof H, White T, Koziol K, Paukner C and Pénicaud A 2017 *Carbon* **111** 142